Effects of large scale eddies and stagnation surfaces on microcrystallization

D.F. Scofield [a], Pablo Huq [b,*]

[a] Department of Physics, Oklahoma State University, Stillwater, OK 74078, USA
[b] College of Earth, Ocean, and Environment, University of Delaware, Newark, DE 19716, USA

ABSTRACT

A Lagrangian marker particle (LMP) method is applied to measure the toroidal large-scale eddies (LSEs) and their enveloping stagnation surfaces in a 280 l bottom-sweeping model crystallizer. The trajectories of a 0.4 cm diameter LMP show that these stagnation surfaces inhibit transport. Analysis shows that the velocity component normal to stagnation surfaces vanish. Therefore, stagnation surfaces act as a semi-permeable barriers to particle transport. Microconductivity measurements show that the stagnation surfaces are leaky at the molecular scale. Thus particle transport through stagnation surfaces is size-dependent. The LMP measurements reveal the structure of the LSEs. This consists of (1) an upward-swirling flow adjacent to the tank perimeter extending from the bottom to the top of the tank, (2) a central, quiescent zone, and (3) a downward return flow between (1) and (2) through a system of nested, smaller diameter, secondary toroidal flows concentric with the impeller axis. A cylindrical stagnation surface surrounds the central quiescent zone. These results are corroborated by measurements of inhomogeneous concentration profiles in an industrial scale 2000 l batch crystallizer. This leads to an understanding of the effects of LSEs on silver halide microcrystal particle size distribution in the industrial scale crystallizer.

1. Introduction

This paper reports Eulerian and Lagrangian experimental measurements of fluid flow in bottom-sweeping impeller batch crystallizers. It also demonstrates the consequence of flow heterogeneity in batch crystallizers. In particular the paper describes the effects of toroidal large scale eddies (LSEs) on microcrystal growth. The study shows how to measure the LSEs and the stagnation surfaces that envelop them. The stagnation surfaces form size-dependent barriers to particle transport because the LSEs and their enveloping stagnation surfaces produce inhomogeneities, e.g., of concentration gradients. This affects the growth of microcrystals and leads to deleterious effects on the particle size distribution (PSD) of the product. The transport associated with LSEs determines macromixing or stirring. Eulerian and Lagrangian computational fluid dynamical simulations by Rielly and Marquis (2001) show that the flow field in crystallizers is composed of such regions (LSEs) of strong mean flow as well as regions of nearly quiescent flow. The LSEs are primarily determined by tank geometry, impeller position, and speed (Tavare, 1995; Brecevic et al., 1986). However, crystal-lization also depends on micromixing and molecular scale reactions (Garside and Tavare, 1985; Tavare, 1989; Söhnel and Garside, 1992; Leubner, 2002).

Experimental results are reported for a 280 l model crystallizer tank in order to identify and to understand the consequences of LSEs and stagnation surfaces. The mixers studied use radial flow impellers. These yield poor mixing in the center of the tank. We also made PSD and concentration measurements in a 2000 l industrial scale tank. The results demonstrate that measurement of stagnation surfaces can be made using a flow follower technique. The one we use is called the Lagrangian marker particle (LMP) method (Scofield and Huq, 2009). The results of these measurements are considered in conjunction with micro-conductivity measurements (Huq and Britter, 1995) to further understand mixing and transport in the tank. We show that stagnation surfaces act as (leaky) barriers to transport for a finite range of particle sizes. This leads to time-dependent, inhomoge-neous mixing of the growing microcrystals and consequent changes in the PSD of the microcrystals. The PSD was measured by a particle-by-particle electrolytic technique based on an instrument called an electrolytic grain size analyzer (EGSA) (Moller, 1970; Holland and Sawers, 1973). The microcrystals of interest here have a mean radius less than 1 μm ($r_{mean} < 1$ μm). The combination of the three measurement methods, LMP, PSD measurement, and microconductivity, usefully char-acterizes the flow and transport in a batch crystallizer and its effect on PSD.

* Corresponding author.
E-mail address: huq@udel.edu (P. Huq).

The motivation of the study was the need to robustly size scale-up, place feed jets, and place control sensors for industrial silver halide microcrystal production in radial flow mixers. The objective of the effort was to produce microcrystals in the scaled-up mixer that had substantially the same photosensitive properties as those produced in the previously used, smaller-scaled radial flow mixer. There was also interest in understanding how these mixers work in general. To develop this more general understanding concepts derived from dynamical systems theory are used (Ottino, 1989). The most important of these for the present work is the concept of a hyperbolic surface. On such stagnation surfaces the velocity field has zero normal direction component. Thus tracer particle trajectories do not cross such surfaces. The contribution of the present work is to show that these concepts involving the dynamical structure of the fluid flow can be useful in achieving scale-up. The work further shows that the Lagrangian marker particle method can be used to better understand the hydrodynamics in a crystallizer and hence uncover mixing mechanisms in stirred tank crystallizers. The paper is of wider application to batch processes in which the PSD of the product is important such as for pharmaceutical products, especially timed-release products.

The paper is organized as follows. Section 2 provides background for the present study and a description of the crystallization process. The theoretical concepts of a stagnation surface and the structure of toroidal LSEs are presented in Section 3. We then provide details of the experimental method for the LMP, microconductivity, and PSD measurements in Section 4. Measurement results are given in Sections 5 and 6. A summary and conclusions section follows.

2. Background

The present paper studies the so-called balanced double jet (BDJ) processes with a bottom sweeping impeller configuration used in making silver halide microcrystals (Gerber, 1982; Wey, 1993; Mullin, 1997). This process is able to produce microcrystals with narrowly distributed variance ($\sigma_{vol} \approx 1\,\mu m$) in the size range of ($0.05-5\,\mu m$). As the name suggests, the process has two feed jets; one for the silver ions (in the form of $AgNO_3$) and another for the halide (in the form of a highly soluble halide salt such as KBr). The placement of the jets is above a bottom sweeping impeller as shown in Fig. 1. This figure also serves to illustrate the model mixing tank in which experiments were conducted. In batch mode operation, seed crystals are started, subsequently the tank slowly fills as new solution is added. The two streams are mixed in the bottom of the reaction vessel, above the impeller, continually forming small grains that, however, are in the presence of larger grains previously formed in the initial seeding of the batch.

Because of the low solubility and small size of the microcrystals, the Gibbs–Thomson–Ostwald ripening process leads to the dissolution of these small grains in favor of the larger ones: small crystallites formed by the micromixing of the $AgNO_3$ and KBr streams dissolve in favor of larger crystallites already present. This "dissolution" process is a surface energy driven process where it is more likely that the small grains dissolve allowing the large crystallites to grow. The control strategy (Gerber, 1982) is to monitor and adjust the concentration of the $AgNO_3$ so that a significant excess of halide is avoided during crystallite growth, as otherwise a wide particle size distribution (PSD) results. As the tank fills different secondary flow fields are formed, changing the LSE structure and therefore the crystal growth. Near the end of a production run, the feed jets are turned off and the microcrystals allowed to continue to grow for a set length of time.
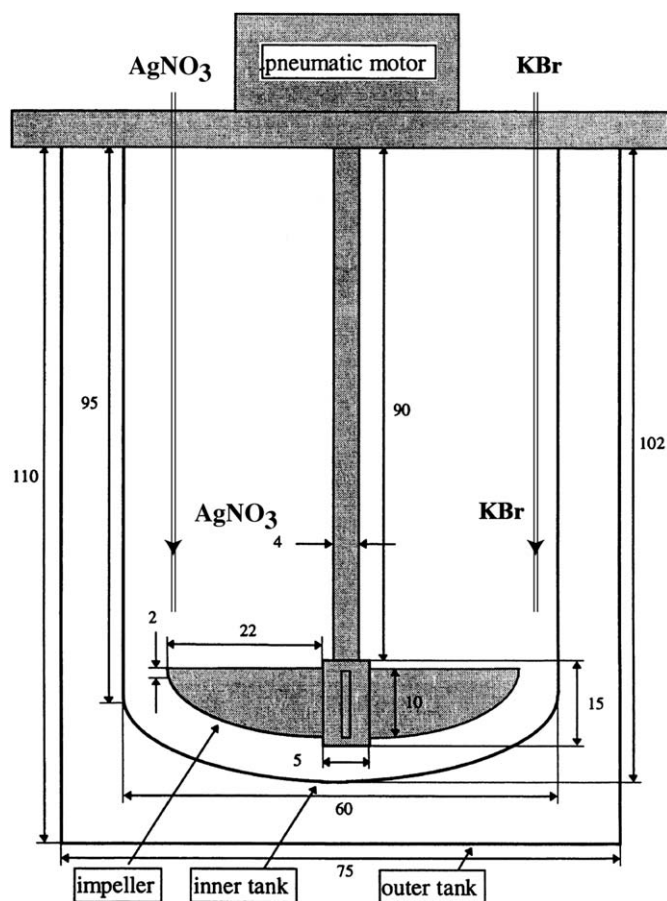

Fig. 1. Schematic of the tank. The dimensions of the 280 l tank. A flat blade (90°, bottom-sweeping) impeller rotating at 50 rpm is used to generate the flow. Shown are the positions of the feed jets. Lengths are given in centimeters.

The description of mixing processes for batch reactors using a bottom-sweeping impeller in the BDJ process is more difficult than for continuous stirred reactors (CSTRs) using a Rushton-type impeller. A schematic of the different LSEs in a Rushton-type reactor and the LSEs in a bottom-sweeping impeller batch reactor is given in Fig. 2. These are time-averaged representations of circulation loops. Note that the large-scale flow structure in Rushton-type mixers (Togatorop et al., 1994) shown in Fig. 2 a has two main toroidal flow regions: one toroidal region above and one below the impeller (Rielly and Marquis, 2001). There is a flow through the center of these toroids that sets up a compensating flow in the remainder of the tank. In the bottom-sweeping batch reactor, the flow is more complicated as indicated in the schematic given in Fig. 2 b. In this case the flow spirals upward along the perimeter of the tank from the bottom and subsequently returns downward. This creates two vertically organized stacks of tori concentric with the impeller axis (Scofield and Huq, 2009). A principal reason for using a bottom-sweeping or near bottom-sweeping impeller is that the bottom placement of the impeller is required for stirring at the beginning of batch crystallization (seeding). The batch process of making $AgNO_3$ leads to significant changes in the height of the flow as the reactor is filled and crystals grown. Results are reported here for a fixed fluid level, having a fixed configuration of toroidal structures. Comparison of baffled and unbaffled tanks showed that baffling caused localized eddies in the lee of the baffles, however, there was little effect on the large-scale flow structure.
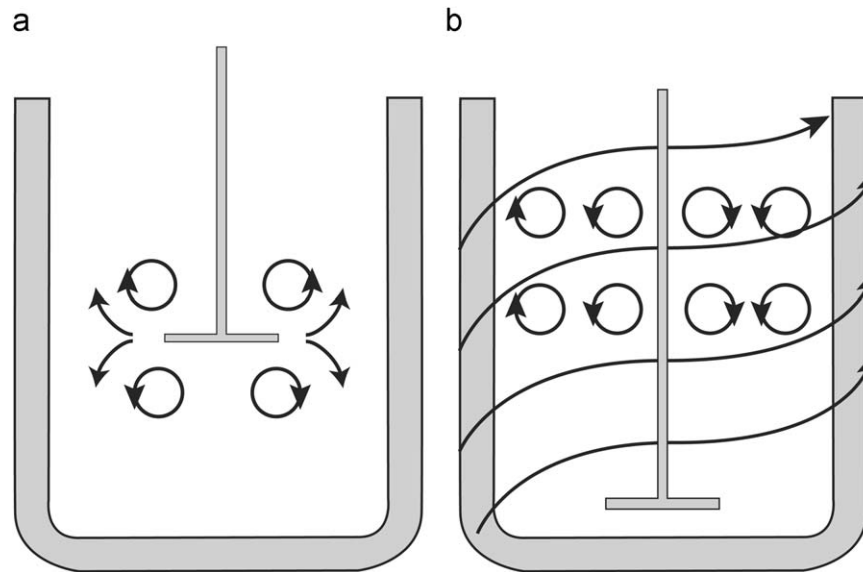
Fig. 2. Schematic of Rushton-type to bottom sweeping impeller flow. (a) The Rushton-type impeller produces upper and lower toroidal flow regions. Rushton-type mixers are generally baffled. (b) The unbaffled bottom sweeping impeller used in this study produces a main inertial flow along the perimeter of the tank returning downward through a stack of nested secondary tori.
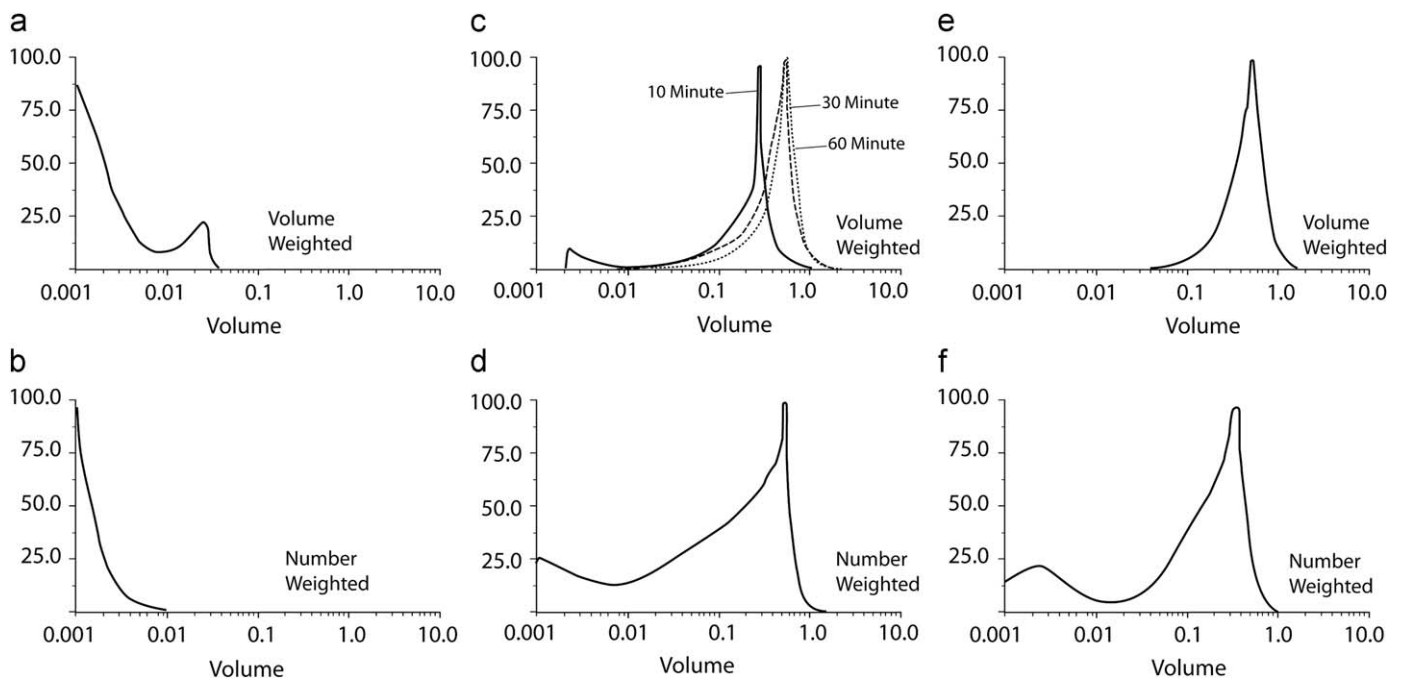

Fig. 3. Probability density function or particle size distribution (PSD) evolution (along ordinate) as a function of volume in a balanced double jet (BDJ) crystallizer after (Gerber, 1982). (a) The volume weighted PSD immediately after initial seed population. (b) The number weighted distribution corresponding to (a). (c) The volume weighted distribution for 10, 30, and 60 min into the production run. (d) Shows the number weighted PSD for 60 min. (e) The narrowly dispersed volume weighted and the number weighted PSDs at the end of the run, after further ripening has occurred and the feed jets have stopped. (f) The number weighted distribution at the end of the production run corresponding to (e).

In a crystallizer, the PSD changes with time as the crystals grow. This is illustrated schematically in Fig. 3 for silver halide microcrystal growth. In this figure the initial PSD shortly after seeding is shown in both volume weighted and number weighted distributions. The evolution of this bimodal distribution is shown as succession of panels as a superposition of the volume weighted distribution at 10, 30 and 60 min into the crystallization process. The final results are shown in the right-hand panels giving the volume and number weighted distributions at the end of the

production run. The smaller mean size part of the distribution is maintained by the addition of new material throughout the growth period. This material grows onto the larger (formerly seed) grains with the number of larger grains remaining the same (Leubner, 2002). A detailed discussion of Fig. 3 is presented in Section 6.

In order to achieve high production yields in the reactor, the $AgNO_3$ and KBr reactant feed streams are highly concentrated (0.5 moles/l) (Chow, 1996). The solubility of AgBr is quite low

(10^{-8} moles/l at 70 °C) and the cubic microcrystals (grains) desired are quite small. Thus, these crystallizers are sometimes called precipitators. In order to keep the microcrystals from coagulating and because of the large size of industrial mixers, the grains are supported in the solution by the presence of dissolved gelatin which forms an emulsion with the grains. With the gelatin support, the solution is stable for hours, and if chilled stable indefinitely. Precipitation would occur without the support of the gelatin solution.

3. Theoretical concepts

3.1. Stagnation surfaces

Stagnation manifolds are regions in fluid flow where the normal component of the fluid velocity vanishes. Fluid flow through these manifolds vanish (zero flux). *Point*, *line*, and *surface stagnation manifolds* are illustrated in Fig. 4. These manifolds can be characterized by their geometry and their (topological) dimension. In the illustrations given in Fig. 4, the topological dimensions of these manifolds or regions are 0, 1, 2, respectively. Fig. 4 a shows a stagnation point. In Fig. 4 b the geometry is that of a line.

Fig. 4 c shows the flow field of interest of the present paper. Here the geometry of the stagnation manifold is a cylindrical surface concentric with the impeller. Note that the large-scale structure of the flow in the tank swirls upward between the tank side-walls and the central cylindrical stagnation surface. The flow returns downward between the side-wall and the stagnation surface as indicated in the figure. The upward swirl of the outer perimeter flow and the compensating downward return flow form a toroidal LSE. Such structure is characteristic of bottom sweeping impeller driven flows in tanks. According to our definition, the walls and top of the flow are also stagnation surfaces since the normal component of the velocity vanishes across these surfaces. The primary flow is tangential, comprising an inner forced vortex surrounded by a free vortex. The LSE surface has the appearance of an inner forced vortex in which there is little transport, except for the effects of secondary circulations in the axial and radial directions (Nagata, 1975).

In order to clarify the notion of a stagnation manifold, consider steady, laminar flow. Here any tube formed from path lines forms a stream tube that is also a stagnation surface since the normal component of velocity to the tube vanishes. Stagnation surfaces measured by the pathlines of large particles embedded in this flow can differ from those measured by the pathlines of molecules or very small crystallites. Very small particles and molecules can easily diffuse or burrow through stagnation lines or surfaces. On the other hand, a larger particle can follow the large-scale structure of the fluid flow if it is not too big. The difference in trajectories between large and small particles is a function of the relative acceleration of the particle compared to that of the fluid. If its acceleration relative to the fluid is large enough, its path will deviate from the path of fluid molecules. This relative acceleration is generally parameterized by the Stokes number (defined later). To reiterate, the cylindrical stagnation surface present in the center of a bottom-sweeping impeller tank flow does not prevent the passage of very small particles to the center of the tank. However, it does act as a barrier to the passage of larger particles.

To understand mass transport and the significance of stagnation surfaces at convective and diffusive scales in the tank, consider the evolution of an aliquot of marker fluid introduced into the tank for the bottom-sweeping impeller tank as schematized in the sequence of Figs. 5a–c. This schematic is based on
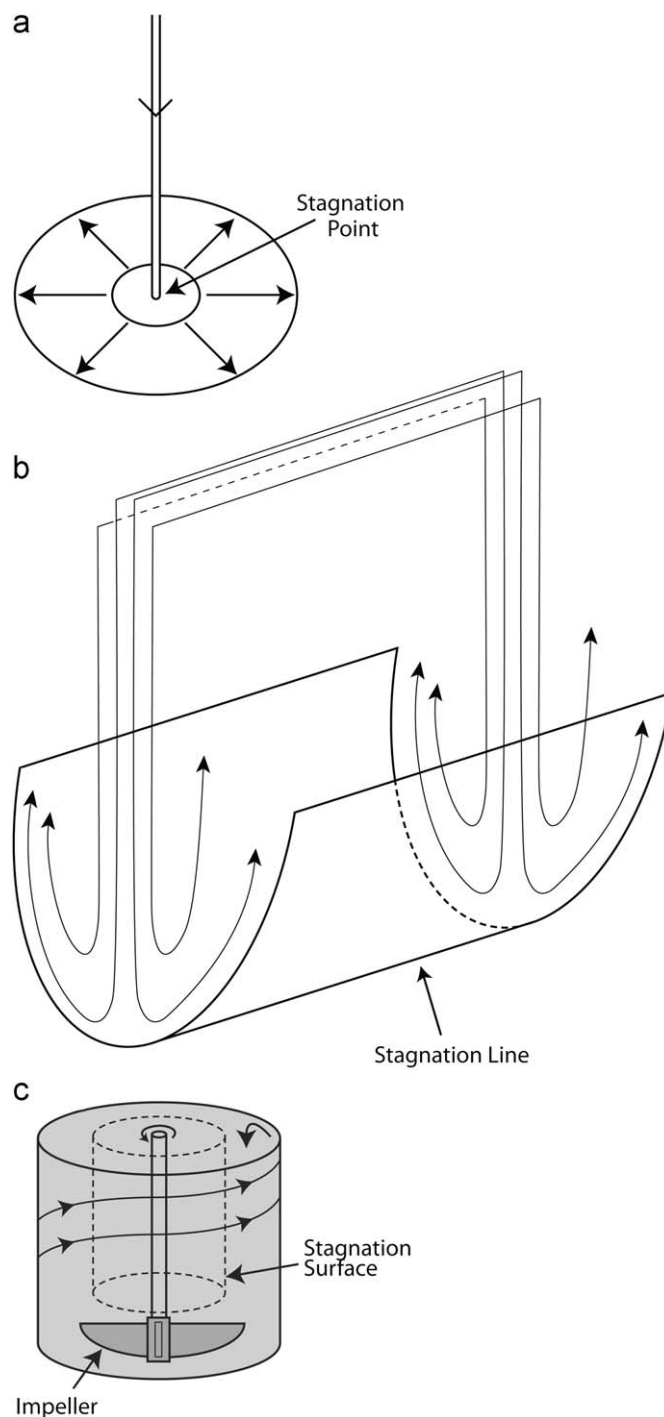

Fig. 4. Schematic of three kinds of stagnation manifolds. (a) Stagnation point, dimension (dim = 0). (b) Stagnation line (dim = 1). (c) Cylindrical stagnation surface (dim = 2). The flow configuration of the present experiment produces stagnation surface similar to (c).

experimental measurements described below. In the schematic, the cylindrical stagnation surface is indicated by the dotted lines. The sequence shows the evolution of a small volume of fluid (marked by dye or salt solution) introduced into the flow at the top of the perimeter of the tank. This marked volume is progressively stretched, folded, and broken-up into smaller and smaller volumes by the stirring of the upward swirling flow at the perimeter of the tank. It rapidly fills the outer annulus; eventually small volumes leak (or diffuse) through the cylindrical stagnation
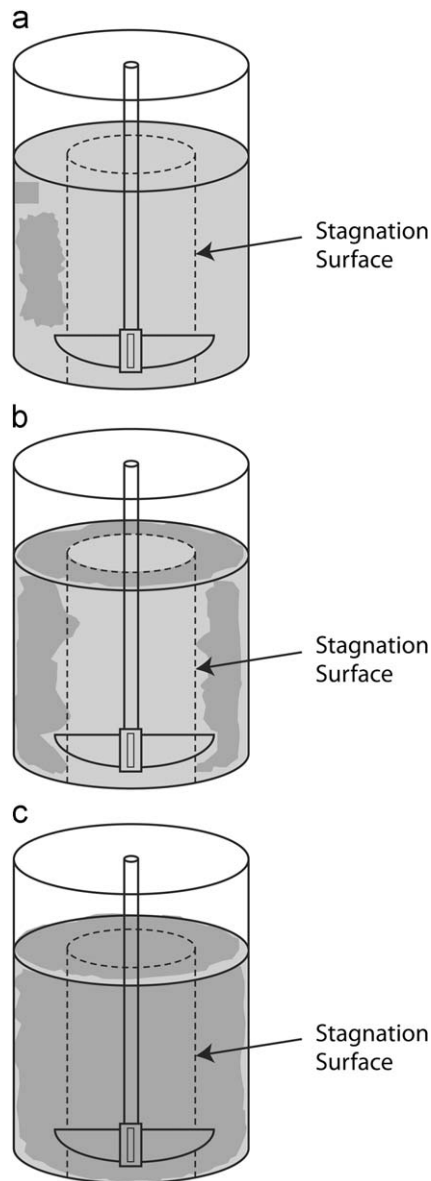
Fig. 5. Schematic of the evolution of a small volume of marked fluid through a cylindrical stagnation surface in a bottom-sweeping impeller tank. Initially (a) the volume is convected in the outer swirl. Subsequently (b)–(c) it also diffuses or leaks through the stagnation surface to the central region.

surface into the center of the tank. Thus, one can think in terms of leaky or porous stagnation surfaces. Note, of course, that the cylindrical stagnation surface persists even after complete mixing or homogenization of the aliquot. Thus, the addition of a new increment of marked fluid will result in another new cycle of mixing. The consequence of the existence of large-scale structure in the tank is inhomogeneous mixing for short times. Eventually, leaks through the stagnation surfaces lead to homogeneous mixing of marked fluid in the tank.

The above flow structure can also be understood in terms of the presence of velocity gradients (that can be computed from the LMP data as described below). There is a velocity gradient $\partial v_\theta / \partial r$ in the free vortex region and hence the marker particle quickly moves in the tangential direction. Within the forced vortex at the center of the tank, there are no velocity gradients so mixing is slower. Secondary effects cause mixing in the axial and radial directions.

3.2. Toroidal flows

There are two basic properties of tank flows that are of interest here. The first is that volume of the fluid in a stirred tank is conserved. The second is that any viscous dissipation is made up by the continual input of energy from the impeller. Thus the flow has many of the properties of a conservative dynamical system. This allows use of tools from dynamical systems analysis. Fluid elements moving in a tank flow necessarily return to the vicinity of their starting point because of conservation of fluid volume. Thus fluid continuity implies that there are large scale toroidal eddy structures in the tank flow. The experimental section demonstrates that such flows actually occur in the tank and influence such properties as the PSD. The characteristics of these toroidal flows are detailed next.

The path of an LMP along a torus flow can be considered from a dynamical systems standpoint (Ottino, 1989; Kambe, 2004). The simplest motion is obtained by taking a bundle of straight, parallel stream tubes in a cylinder section as indicated in Fig. 6a. This shows a bundle of straight stream tubes like a bundle of spaghetti. Twisting and joining these gives a torus connection of stream tubes illustrated in (b). The particles in each tube circle the center of the torus once. This is a simple torus flow. A more complex flow occurs when the bundle of stream tubes is rotated by 180° in
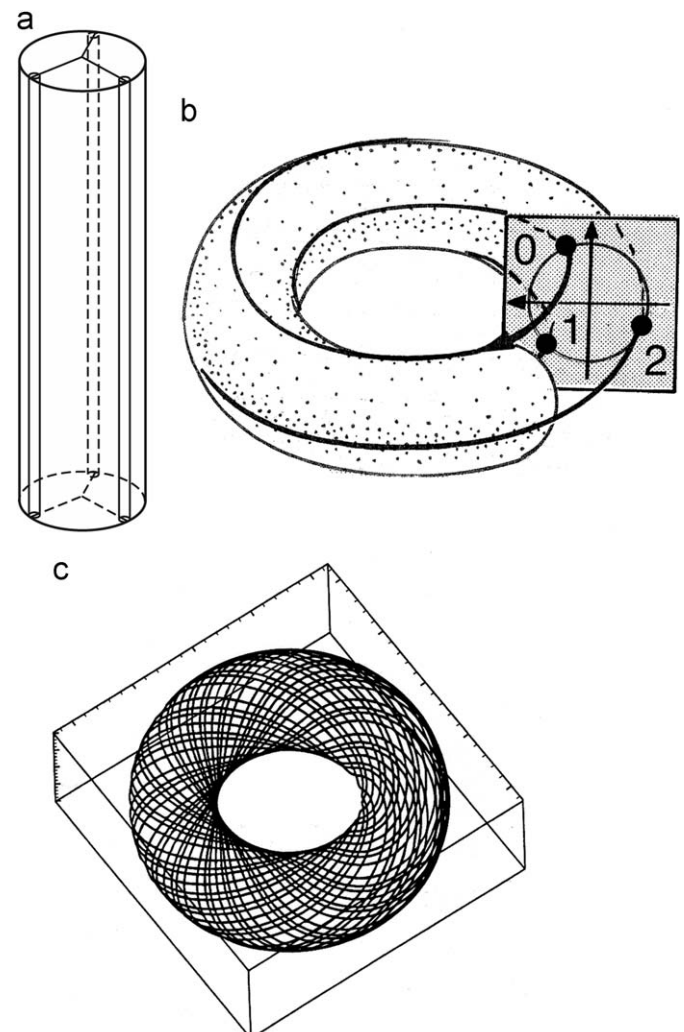

Fig. 6. Trajectories on a torus. (a) A system of straight stream tubes. (b) The result of twisting and joining this system of tubes. (c) A quasi-periodic orbit beginning to completely cover the 2D torus surface.

cross-section or meridian before joining them. Such flows can be described by the integers p and q. In the present case, it takes a LMP two cycles, $q = 2$, along the long path or longitude to return to its initial position but at the same time the LMP rotates around the short radius meridian one time, $p = 1$. We call this a $L_{p,q} = L_{1,2}$ torus flow. Next consider making the angle 120°. Now it takes $q = 3$ cycles along the longitude and in the same time $p = 1$ meridional cycles have occurred. This is called a $L_{1,3}$ torus flow. To increase the meridian cycle rate, one adds another complete meridional cycle or twist of 360° of the cross-section giving a total twist of 480°. The Poincaré map, illustrated on the shaded Poincaré section in Fig. 6 b, has a sequence of $0 \rightarrow 2 \rightarrow 1$ and repeats for another cycle around the torus. The trajectory through this twisted system of stream tubes cycles two times around the meridian while completing three cycles around the longitude of the torus making a $L_{2,3}$ toroidal flow. In Fig. 6 c a quasi-periodic orbit is shown as it begins to completely cover the 2D torus surface. This occurs when (p, q) are not relative prime numbers. The trajectory is quasi-periodic. The Poincaré section points merge onto a circle. Such periodic trajectories on the torus are characterized by turning rates p/q where p and q are integers with no common factors. Such factors are said to be *relatively prime*, the greatest common divisor of p and q is unity. When (p, q) are relatively prime the trajectories yield a finite number of points on a circle in the Poincaré plane.

The trajectory on a torus can also be expressed mathematically in terms of the parametric representation of the LMP motion in three dimensions (Kambe, 2004, p. 47):

$$x_1 = (R + r \cos 2\pi p t) \cos 2\pi q t, \tag{1}$$

$$x_2 = r \cos 2\pi p t,$$

$$x_3 = (R + r \sin 2\pi p t) \sin 2\pi q t. \tag{2}$$

The longitudinal radius is R and the meridional radius is r. As t varies from 0 to 1, the meridional angle cycles p times and the longitudinal angle cycles q times. This describes a so-called $T_{p,q}$ torus knot. For relatively prime integers p and q, the motion is a periodic orbit on a toroidal shell (meridional radius r) of a torus flow as described above. That the flow stays in a toroidal shell of radius r is seen from the fact that in forming the flow manifold one twists a tube of radius r about the cylindrical axis. (See Fig. 6 a.)

An important new behavior of the LMP orbit on the torus occurs when (p, q) in Eq. (1) are *not* relatively prime integers, say p is an irrational. This leads to an infinite number of points on the Poincaré plane organized on a circle. To understand this, let p be irrational but close to a prime p' and q be relatively prime to p'. Then the motion of an LMP going around the torus is perturbed, so that it is a little out of phase when it returns to the Poincaré plane, cutting the torus along a meridian. This leads to a displacement along the circle drawn through the points on the Poincaré plane that would be generated by the nearest relative prime (p', q). Eventually this displacement accumulates so that all of the infinite number of points on the circle drawn through the relatively prime points are hit. This leads to a Poincaré section containing a myriad of dots along the circle (Ottino, 1989, p. 143). The trajectory of the LMP now completely covers the torus surface as is seen in Fig. 6 c. Such motion is called quasi-periodic.

This situation can become more complicated for trajectories not constrained to a 2D surface. In this case, the flow can be enveloped by a toroidal stagnation surface but the flow trajectory can fill nearly the whole solid torus. Such flows are called chaotic. The Poincaré section described above then fills in with dots. The experimental fluid flow whose results are reported in this paper is even more complex than a chaotic dynamical system on a 3D
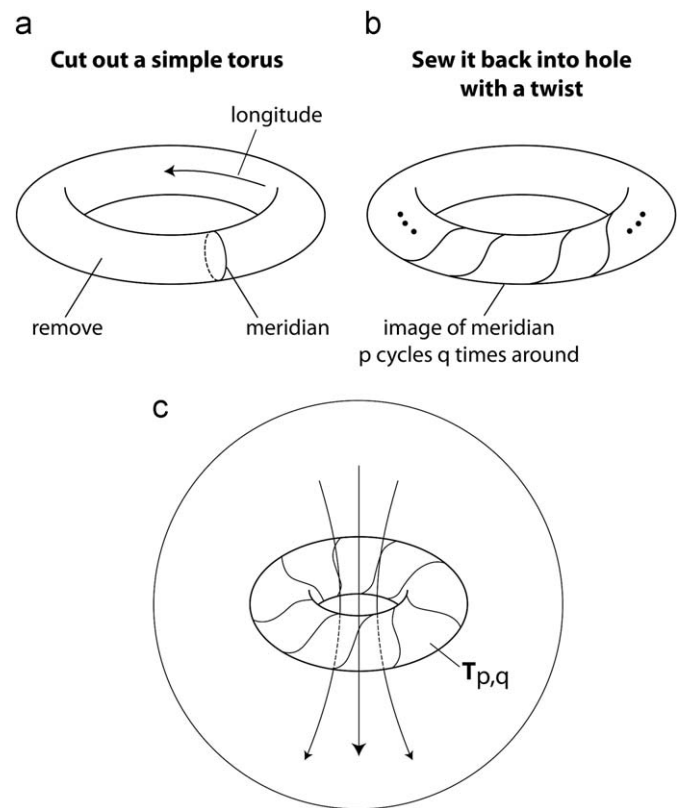

Fig. 7. Constructing the flow on a $L_{p,q}$ torus flow. (a) A simple torus is cut out of the fluid in the tank. It is then, cut, twisted and pasted together as in Fig. 6 a, making sure that the stream tubes are joined seamlessly. (b) This shows a perimeter $L_{p,q}$ toroidal path. (c) Then it is pasted back into the tank fluid in a way that the background fluid moves in concert with the cutting, twisting and pasting of the $L_{p,q}$ torus flow.

torus. A description of such chaotic flows requires more than two degrees of freedom (Ruelle and Taken, 1971a, b).

The topology of the toroidal systems of the flow is illustrated in Fig. 7. This figure describes a flow on the (stagnation) surface belonging to a primary $L_{p,q}$ toroidal flow. The continuity constraint is used to construct this flow by cutting out a simple torus in the liquid of the tank as shown in Fig. 7 a. This torus is then twisted and joined at its ends to form an $L_{p,q}$ torus as illustrated in Fig. 7 b. Finally it is "sewn or pasted" back into the remainder of the flow in a way that a meridian lies on the curve that cycles p times around the torus as it runs q times around the longitude. This procedure satisfies the continuity constraint for the interior of the primary toroidal flow. For the remainder of the fluid, continuity requires connecting the remainder in such a way that the velocity normal to the $L_{p,q}$ stagnation surface is continuous. This can be accomplished by dragging the surrounding fluid along with the $L_{p,q}$ surface inducing a flow in the surrounding fluid as indicated in Fig. 7 b. This forms the *associated flow* $L_{q,p}$. In Fig. 7 c this associated toroidal flow is illustrated by the flow lines going through the central region of the *primary toroidal* flow. These lines join to form closed particle lines of the associated toroidal flow. For every toroidal flow in a tank there is another associated toroidal flow enveloping it. A stagnation surface separates the two. Because of the continuity of the velocity field, the velocity field normal to the stagnation surface between these two toroidal flows must be continuous.

This "cut and paste" construction when extended to multiple LSEs leads to the possibility of a sequence of trapping scenarios. This occurs when the LMP leaks through a stagnation surface, then becomes trapped in another. If we consider the time it takes

the LMP starting at a certain toroidal LSE to return to a region in that torus, it is found that a consequence of multiple torus flows is a distribution of return-times with short return-times within a single torus and longer ones where the LMP is trapped in winding trajectories around other tori. In the latter case there could be substantial time before the marker particle returns to its original torus. This results in a complex return-time distribution as found in our experimental measurements.

4. Experimental methods

Experimental measurements were undertaken on two tanks. The LMP and microconductivity measurements were done on a model 280 l bottom-sweeping, four-bladed impeller driven tank flow diagramed in Fig. 1. The model tank has a height 102 cm and is 60 cm in diameter. The impeller is powered by a constant power pneumatic motor to generate a flow with constant energy dissipation. The bottom-sweeping impeller rotates at 50 rpm. Reynolds number at the blade tip exceeds 25,000, so the flow is turbulent. This degree of agitation does not preclude the existence of LSEs as described below.

To check the dependence of the large scale structure of the flow with respect to parameter changes, the speed of the impeller was varied by $\pm 20\%$ and baffling was introduced. In addition to the flat, 90° bladed impeller, measurements were also made using an impeller with 45° blades. The form of the large-scale structure of the flow for both impeller configurations is similar. Namely, that there is a quiescent zone in the center of the tank, bounded by a cylindrical stagnation surface. We also conducted experiments on baffled tanks. For this, the four baffles were 8 cm wide and extended from just above the impeller to the top of the tank. The ratio of the width of the baffles to the tank radius is 0.27. The principal change in the flow field was some recirculation in the lee of the baffles. Thus, even for these variations, similar patterns of large scale flow structure (tori) and stagnation surfaces were found.

All PSD results derive from measurements using 2000 l production scale tanks. The routine sampling point during a process run is near the top of the fluid in the tank, just below the top surface and near the tank wall. An experiment was also performed on the 2000 l production scale tank whose impeller was not bottom-sweeping. In this case the impeller was located about 20 cm above the bottom.

4.1. Lagrangian marker particle measurement

Three orthogonally placed digital cameras were used for tracking the LMP. The use of a third camera allowed correction for distortion along the line of sight due to the impeller shaft, impeller, or baffles when present. The clear Plexiglas^{TM} model tank was surrounded by flat surface Plexiglas^{TM} "aquarium" to reduce optical aberrations. Data sets for the LMP for up to 100 h duration were used in the analyses (Scofield and Huq, 2009).

The size and buoyancy of the LMP are, of course, an important consideration of the LMP measurement method. Our choice of size was made on the basis that a wide view of the whole tank (1 m by 1 m) was needed and it was desirable that the LMP be as small as possible given the resolution of the imaging system (Scofield and Huq, 2009). Considerations with respect to the efficacy of flow following have been elucidated by Maxey and Riley (1983), Maxey (1988) and McLaughlin (1988) who show that a neutrally buoyant Lagrangian marker particle (LMP) with Stokes number ($St = 2a^2 U/9vL$) less than one would be expected to be a good flow follower. The LMP radius is denoted by a, L is a characteristic length scale that is chosen to be the radius of the tank (30 cm for

small tanks and 60 cm for the larger tank studied), U, a characteristic velocity of 30/cm s^{-1}, and v the kinematic viscosity of water, 0.01 cm^2 s^{-1}. The LMP is 0.4 cm in diameter and made of a neutrally buoyant mixture of carbon black and bee's wax. The value of the Stokes number is less than one in both the 280 and 2000 l tanks. The LMP size is similar to that used by Wittmer et al. (1995) and Wittmer (1996) in their study of the flow in a Rushton-type mixer.

The inertial dynamics of particles was further examined in Haller and Sapsis (2007) and Babiano et al. (2000), who showed that near a stagnation point, if a particle had large enough inertia, it would not follow a fluid path line. Instead, the particle would be excited to a new flow manifold and it would return to the main fluid flow manifold at a rate proportional to the inverse of the Stokes number.

These results imply that the larger the particle's inertial deviation from the flow's the larger the relaxation time required for it to again follow the path of the fluid. Generalizing from points to surfaces, one recognizes the possibility of inertial transport through the stagnation surface by very large particles and diffusion by very small particles. Intermediate sized particles, however, are sensitive to the presence and geometry of the stagnation surfaces. The problem of experimentally identifying and locating the stagnation surfaces then comes down to finding a neutrally buoyant particle size that is neither too large nor too small.

4.2. Microconductivity measurement

The microconductivity probe consists of a small orifice in a sapphire bead placed at the end of a tube through which a sample is continuously pulled for conductivity measurement. The probe is calibrated in a salt solution by comparing to a hydrometer as a control. The comparison allows one to determine the output voltage of the driving electronics and signal conditioning circuitry. A linear output is found for the range of concentrations used in the experiments. The frequency response ranged from DC to 100 Hz. The spatial resolution of the probe, of the order of 0.1 mm, resolves down to the Kolmogorov scales of the flow.

In the microconductivity measurements presented, a 1 l volume of salt solution of density 1100 kg/m^3 is released at the top on the tank at the side-wall. The microconductivity probes are located at opposite sides of the tank. Measurements are taken at two locations each at 25 cm above the bottom of the tank but at radii of 10 and 20 cm from the impeller shaft. Best fit, sixth order polynomials, are fitted to the individual time-series to aid interpretation.

4.3. Particle size distribution measurement

A standard method for measuring the particle size distribution in silver halide crystallite manufacture is the EGSA. Other methods are reviewed in references Mullin (1997) and Allen (1997). In the electrolytic method, the crystallite particle size distribution (PSD) is measured via a particle-by-particle electrolytic reduction to Ag from a dispersed sample of the emulsion diluted in a Na$_2$CO$_3$ electrolyte as first described by Moller (1970) and later by Holland and Sawers (1973). The device used for our measurements is an improvement of the instrument described in reference Holland and Sawers (1973) and uses a platinum wire probe of 10 μm diameter centered in a flattened tip glass support. A small sample of microcrystals are dispersed evenly over a filter paper and placed in a holder filled with the electrolyte (0.002 N KBr; 0.05 M Na$_2$CO$_3$, pH = 11.4). The probe is placed on the filter paper containing the dispersed crystallites in the presence of a

pool of the electrolyte. The cylindrical crystallite holder rotates about its center at a slow rate (1 rev/h) and the probe placed at a 3 cm radius.

A current pulse is created when a microcrystal encounters a silver halide grain. A potential difference between anode and cathode of greater that 0.25 V is applied to drive the reduction/oxidation creating the pulse measured by the external circuitry. Reduction of Ag^+ in a microcrystal occurs at the Pt cathode and oxidation of the halide at the counter-electrode anode. The maximum currents measured range from 1 to 10^4 μA. These currents are converted to a voltage signal through a resistor network and then converted using a fast analog-to-digital converter for numerical analysis.

The digitized pulses, representing the current required to electrolytically decompose a microcrystal, are related to equivalent spheres corresponding to the cubical crystals. The pulses are analyzed in real-time to eliminate various sources of multiple pulses so that only well formed pulses remain. The pulses that remain after screening are accumulated and placed into a histogram from which statistical properties of the PSD can be numerically computed. Using a series of overlapping ranges, the device can measure grain volumes from 10^{-5} to 10 μm^3. Approximately 5000 particles can be measured in 5 min. The results of the analysis have been checked using electron-micrographic methods. For the smaller grain sizes, the apparatus is isolated from acoustic vibrations by mounting it on an active vibration isolation table; thermal and electromagnetic noise is also carefully filtered out of the environment and the signal. This measurement method is sensitive enough to measure the impact on the PSD due to changes in feed jet position, concentration rate programming (Mumaw, 1985), etc.

5. Measurements of large scale eddies and stagnation surfaces

The large-scale flow structure in the tank consists of an inertially driven, spiralling upward flow at the perimeter of the tank that almost isolates a central quiescent zone concentric with the impeller shaft. In addition to the upward perimeter swirl, there is a compensating downward return flow that occurs in the region between the stagnation surface and upward swirl. This forms the main toroidal flow or largest LSE in the tank.

To analyze this flow, the Poincaré sections of the impingement points of the LMP trajectory through horizontal and vertical cross-sectional planes can be made as shown in Fig. 8. The Poincaré sections vividly portray the different regions of flow in the tank. Ten hours of data are used. In Fig. 8 a, the data are shown in plane or horizontal cross-sectional view orthogonal to the impeller shaft. There is a near absence of trajectories in the central quiescent zone. The absence of points in this region suggests different dynamics than that found in the outlying regions. We refer to this region as the *central quiescent zone*. This quiescent zone is also seen in the side view, Fig. 8 b. It is evident that the LMP rarely crosses the boundary of the quiescent zone. This implies that this boundary is a stagnation surface. The geometry of the stagnation surface surrounding the quiescent zone is a vertical cylinder of radius approximately 10 cm.

The Poincaré sections of Fig. 8, except for the central quiescent zone, are uniformly populated with dots. The physical implication of the uniformity of dots is an indication that the scales of the spatial fluctuations are smaller than those of the main toroidal swirl (the main LSE whose scale is of the order of the tank size). There is an intermingling of crossing sense (plus signs and dots) in the region near the central quiescent zone associated with the secondary toroidal flow.

Our experiments showed furthermore, on the rare occasions when the LMP entered the central quiescent zone, that the LMP drifted around circularly and downward for a few cycles until it reached the proximity of the stagnation surface whereupon it quickly exited the central zone. This behavior, whereby the LMP exits more readily from the quiescent zone than it enters, shows that the dynamics of the LMP in the vicinity of the stagnation surface is asymmetric with respect to the stagnation surface. If the barrier to transport were symmetrical, then given enough time, there would be just as many LMP trajectories in the central quiescent zone as outside.

The near absence of trajectories in the quiescent zone can be understood as follows. If the LMP entered the central region and did not exit, it would produce a space-filling path in the central region. From Figs. 8 a and b, it is evident that this is not the case. Thus, the LMP is not trapped in the central region after entry. In fact, it is mostly trapped in the outer swirl and spends little time in the central region. In the nomenclature of dynamical systems analysis, this results in the central region "repelling" the LMP. The vertical Poincaré section of Fig. 8 b also shows that the upward LMP trajectories reside primarily in an annular region near the perimeter of the tank. Note that the number of points in the central quiescent zone increases toward the bottom of the tank. This arises from the greater leakage near the impeller due to larger local accelerations. The fact that there are some trajectories that enter the quiescent zone indicates that the stagnation surface is leaky.

Fig. 8 c shows a vertical Poincaré section for the case of a 45° impeller. As seen in Fig. 8 c compared to Fig. 8 b, there is a greater degree of transport of the LMP into the central zone for the 45° impeller case, as indicated by the greater density of dots there. From Figs. 8 b and c it is also evident that the radius of the stagnation surface bounding the quiescent zone increases as one moves from the bottom of the tank to the top. In general, the overall large-scale structure of the flow in the two arrangements is similar in form.

The Eulerian velocity components in the tank are given in Fig. 9. These quantities were computed by averaging a typical 3 h segment of Lagrangian velocity data along the LMP path as it passed through the mid-height region in the tank. The flow structure illustrated is typical, although there are variations between each 3-h-averaged result. Surrounding the impeller shaft is the quiescent zone that the LMP rarely visits. Adjacent to the quiescent zone for $11 < r < 16$ cm is a shear flow region containing secondary tori. Following this for $16 < r < 20$ cm is a region of downwelling flow (as indicated by the negative values of v_z) and another shear flow region ($20 < r < 22.5$ cm) also containing secondary tori. Finally, there is a region of centrifugally driven upwelling flow at the perimeter of the tank as shown by the large upward v_z- velocity field components in the vicinity of the perimeter wall near $r = 25$ cm. Tangential velocities v_θ varied approximately inversely with radius $v_\theta \approx 1/r$ between the perimeter and the region of shear ($12 < r < 20.5$ cm). This inverse relation is similar to that found for a free vortex (Nagata, 1975).

The shear of the downwelling flow creates two systems of secondary tori at the boundaries of the downwelling flow. The signature of secondary tori is fluctuating velocities in this region. The outer stack of tori is centered at $r = 21$ cm. The scale of the tori is about 2 cm and they occupy the region between $r = 20$ and 23 cm. There is also region of secondary tori centered at $r = 13$ cm associated with the shear of the downwelling flow. These tori also have a scale of 2 cm. They occupy the region between $r = 12$ and 15 cm. The horizontal range of positions of both sets of secondary tori is greater than their scale. This indicates that they translate horizontally, thereby accounting for the fluctuations in the
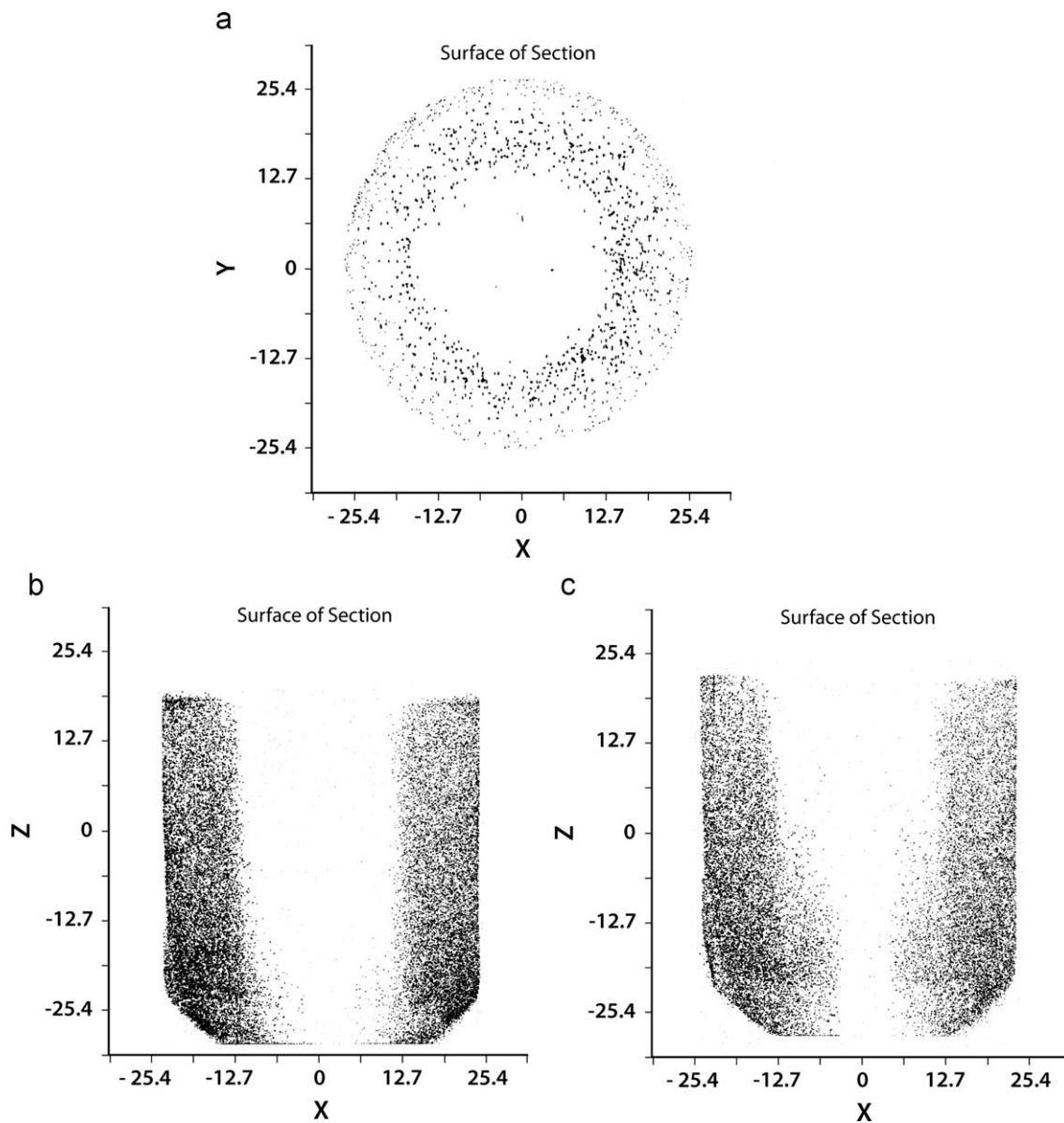
Fig. 8. Poincaré sections of the LMP trajectories in unbaffled mixing tanks. Axes units are centimeters. For (a) and (b), 90° vertical blade impeller. The symbols indicate a particle path crossing through a plane (Poincaré section) in cross-section view. The plus signs are associated with downward and the dots with upward crossings through the Poincaré section. (b) The side view perspective shows the vertical structure of the flow and the quiescent central zone. (c) Poincaré section for the flow using 45° tilt impeller blades.

measured Eulerian velocity in these regions. The motion of the secondary tori results in variations in the LMP trajectory. The Poincaré section reflects this by producing points in an irregular pattern. Averaged over time, this leads to the uniformity of the Poincaré sections of Fig. 8. There is a large region of essentially vanishing velocity at the center of the tank.

The Poincaré sections and velocity profiles just described reveal that a dynamical consequence of the stagnation surface surrounding the central quiescent zone is trapping of the LMP in the largest LSE composed of the upwelling perimeter flow and compensating downwelling return flow. Similar trapping of the LMP also occurs in the secondary tori when the LMP leaks into a secondary torus.

An example of a trajectory showing toroidal motion and trapping in secondary tori is given in Fig. 10. The data presented show that the LMP is trapped for about 38 s at a mean height of $z = 25$ cm with undulations of amplitude of about 2.5 cm. There are about six cycles to these undulations in the 38 s time interval

in which the LMP is trapped in a (secondary) toroidal trajectory. Thus the meridional cycle period is about 6 s. During this interval the z-position undulation reflects motion along a single small $L_{p,q}$ toroid. This trapping localizes the LMP to a small tori until it escapes after about 38 s. (From Fig. 9, the tangential velocity v_θ is 40 cm/s at a radius of 12 cm. Thus the period required to complete a longitudinal circuit around the impeller shaft is about 2 s. The meridional period is about 6 s. This ratio of periodicities describes a (1,3) torus path. Other paths such as (1,2) are also found.) The LMP then undergoes a large downward acceleration and the trajectory of the LMP at the right-hand side of Fig. 10 at $t = 38$ s, suddenly drops while it escapes from the secondary torus. This trapping/escaping behavior is repeated throughout the upper reaches of the flow and leads to multiple paths from the circumferential flow region along the top of the main swirl to the bottom of the tank. This leads to a complex return-time distribution as discussed below. This distribution provides a basis for computing the time it takes for the tank to be homogeneously
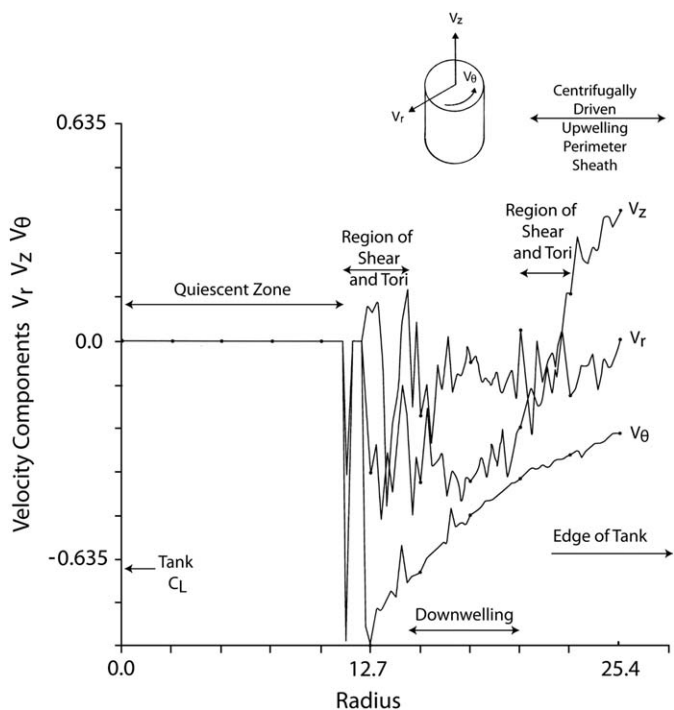
Fig. 9. Computed average Eulerian velocities at mid-height of tank ($z = 0$). Along the vertical axes are the radial velocity v_r, the vertical velocity, v_z, and the azimuthal velocity, v_θ, in units of meter per second (m/s). Along the horizontal axis is the radius in units of cm.
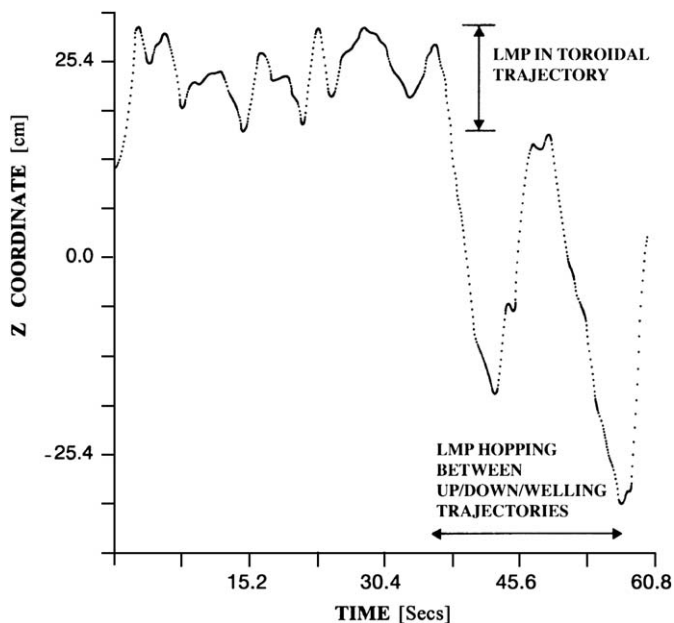

Fig. 10. Time series of LMP trajectory caught in a secondary torus flow. Shown is the projected height of the LMP as a function of time. The first part of the series shows motion along a single $L_{p,q}$ toroid centered at a height of about 25 cm. The last part of the series shows a downward transition along the inner part of the main toroidal flow.

mixed. Such a blending or homogenizationation time can be used to characterize mixing efficacy (Bai et al., 2007).

To further understand material transport in the tank, micro-conductivity measurements were performed. These consist of introducing salt solution in the perimeter swirl adjacent to the tank wall and obtaining microconductivity time series at two

locations: at the outer upward perimeter swirl A and at the quiescent center B as shown in Fig. 11. For time series A, the microconductivity measurement before 15 s shows large concentration fluctuations (deviations from the trend lines of the best-fit polynomial). The magnitudes of the fluctuations are initially of the order of the mean concentration ($\sim 1\%$) and relatively long lived in duration (2–3 s). Both the magnitude and duration of fluctuations subsequently decay with time. After 20 s, the concentration fluctuations are vanishingly small indicating a steady state or well-mixed concentration field. The evidence from the return-time distribution and the presence of the quiescent zone and the stack of tori indicate that the flow is, in fact, not well mixed on this time-scale of 20 s.

In time series B, the salt solution added in the perimeter is measured in the quiescent zone. Salt is slowly advected from the perimeter zone into the central quiescent zone and attains a nearly stationary value after 60 s. There is an absence of large fluctuations in the central quiescent zone. Rather the fluctuations are small in magnitude and duration (i.e., size) throughout the whole 60 s time interval. The rise of concentration is cumulative error function-like, consistent with a diffusive-like scalar field. Even though the scalar source is located in the perimeter swirl, fluid molecules of the scalar continually reach the quiescent central zone indicating a leaky stagnation surface adjacent to the quiescent zone. The concentration evolution at the two locations differ, reflecting the different mixing dynamics at the two locations.

Diffusive-like mixing occurs in the central region whereas both diffusion and large-scale convective transport (stirring) occur in the perimeter swirl flow. These regions are separated by stagnation surfaces. The Poincaré section of Fig. 8 shows that the leakage rate at the scale of the 0.4 cm diameter LMP is quite small (only a few paths are found in each 3 h sample of the data set comprising the Poincaré section data of Fig. 8). So, the time to achieve homogeneous mixing of particles of the scale of the LMP can be quite large. This contrasts with the larger leakage rate measured at the resolution scale of the microconductivity probe where homogeneous mixing is achieved in times of the order of 60 s. Thus, the leakage rate depends on the particle size.

From the LMP data, one can measure the travel time along a trajectory in the fluid from any point to another. This time depends on the actual path taken in the turbulent flow in the tank and leads to a distribution of return-times. The resulting return-time distribution (RTD) contains information on the large-scale structures of the flow. The return-time distribution for the LMP starting and returning to a plane just above the impeller in the 2801 tank is given in Fig. 12. The time interval is plotted along a logarithmic scale. The distribution is composed of two log-normal parts: one generated by shorter-time paths (typically 2 s) whose trajectories are depicted in the left inset and another, depicted in right-hand inset, for longer-time (typically 15 s) trajectories. Short-time paths belong to the left part of the distribution. These paths as shown in the left inset of Fig. 12 follow the main swirl from bottom to top and return. They do not involve trapping in secondary tori. Moreover, they lead to more rapid crystal growth because these paths involve a greater frequency of return to the region of the reactant feed jets. The longer return-time paths, such as those shown in the right-inset, arise because the LMP becomes trapped in secondary tori. Return-times of such trajectories can lead to return-times of up to 80 s. The trapping leads to the long return-times of the right-hand log-normal curve.

In summary, the LMP data show a main toroidal flow and a central quiescent zone. A stack of nested tori is embedded in the shear zones adjacent to the quiescent zone and adjacent to the upward perimeter flow. The LMP generally follows paths that do not cross the stagnation surfaces. The microconductivity results show that the stagnation surfaces are quite leaky at molecular scales.
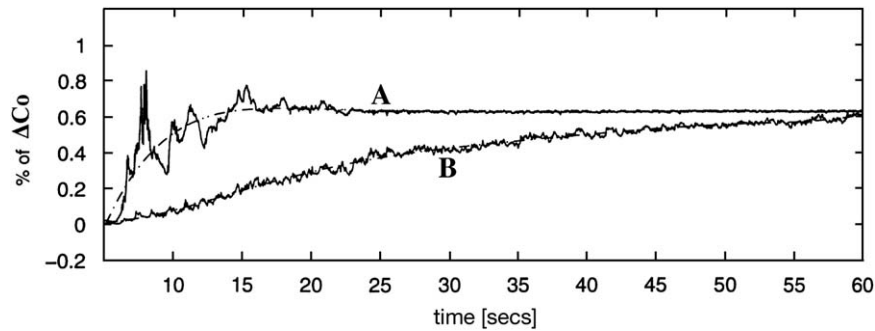
Fig. 11. Microconductivity results for an aliquot of salt solution introduced near tank sidewalls at the top of the tank. (a) Microconductivity signal outside the central quiescent zone. (b) Signal inside the central quiescent zone.
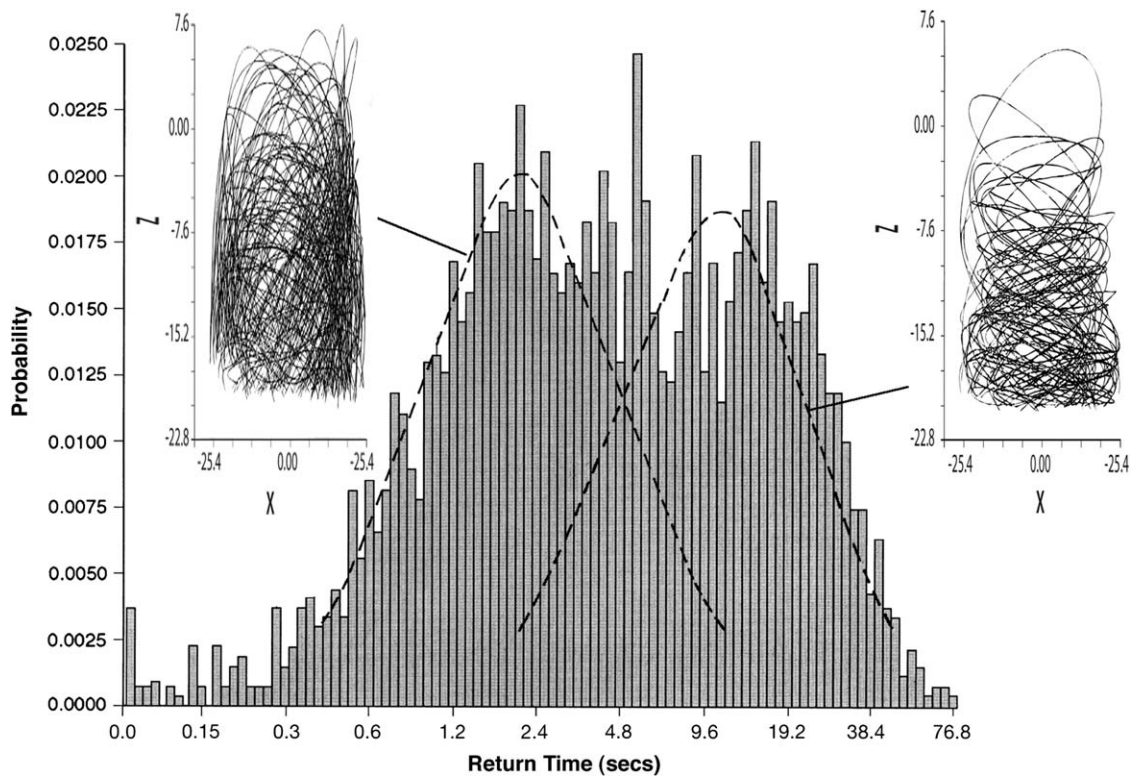

Fig. 12. Return-time distribution of LMPs. Shown is the return-time for LMPs starting and returning to a plane just above the impeller. (a) The distribution is approximated by the sum of two log-normal return-time sub-distributions. (b) Shown in the left-hand inset are typical LMP trajectory for left sub-distribution. These return-times are short, averaging about 2 s. (c) Shown in the right-hand inset are typical trajectories for the right-sub-distribution. These return-times are long, ranging up to 80 s.

One concludes that (leaky) stagnation surfaces and toroidal flow zones lead to size-dependent, spatial and temporal segregation of particles in the tank. Such non-uniform mixing zones lead to variations in particle histories causing changes in the PSD. The spatial segregation leads to different Gibbs–Thomson–Ostwald growth rate in each tori. As the tank fills during the batch process, the main swirl envelopes increasing numbers of secondary tori. This leads to a temporal dependence of mixing efficacy and consequently a time-dependence in the PSD additional to that derived from the Gibbs–Thomson–Ostwald growth alone.

6. Effects of large scale eddies and stagnation surfaces on PSDs

The visual appearance of the fluid throughout the 2000 l tank is a uniform opaque yellow chiffon color due to the suspended silver halide grains. There is no visual demarcation between the central quiescent zone and the perimeter swirl flow. This can be understood to be a consequence of the transport through the stagnation surface bounding the central quiescent zone as shown by the LMP and microconductivity measurements

We now consider effects of stagnation surfaces and LSEs on the PSD. Fig. 3 shows the evolution of the PSD during the process of crystallization. The plot is a probability density function with the ordinate giving the percentage of the total belonging to a certain volume range. The upper panels are volume weighted and the bottom ones are number weighted. Consider the development of the initial distribution after 10 min of growth. In the growth process, small particles in the left part of the distribution dissolve and via the Gibbs–Thomson–Ostwald ripening process leads to growth in the main part of the distribution to the right. The largest peak is from Gibbs–Thomson–Ostwald ripened grains that continue to grow in the flow described. As the tank fills, the continually growing grains increase in mean size as shown by the evolution of the main peak in the PSD. The smaller peak to the

left of the main peak, most easily seen in the number weighted distribution, is due to the microcrystals continually forming in the region of the feed jets. In the intermediate time period (10–30 min) shown in the center panel, the main peak narrows as the PSD shifts to larger mean size. It is seen that during ripening that the peak of the PSD continually moves to the right. Finally as shown in the last panel, after the feed jets are stopped (after 60 min and a subsequent ripening hold time), almost all the volume of the very small grains dissolve onto the larger ones via the Gibbs–Thomson–Ostwald process. This removes their part of the distribution. Small grains remain (as seen in the volume weighted distribution), but their volume is small as seen on comparing the final number weighted to the final volume weighted distributions.

The intermediate time deviations of the PSD from single mode log-normality in Fig. 3 can be understood to arise from inhomogeneous mixing and the Gibbs–Thomson–Ostwald ripening process. In the center panel of Fig. 3, there is present a large number of small particles that have grown from the local precipitation directly involving the feed jets. These form the part of the distribution on the left of the main peak in the number weighted distribution found in the lower half of the figure. The growth history of these particles differs markedly from those particles in the main part of the distribution. The main part of the PSD can be attributed to particles having paths like those in the left insert of Fig. 12. Such paths subject their growing crystallite to the most intense Gibbs–Thomson–Ostwald ripening because of their repeated proximity to the feed jets. As the 2000 l tank fills, transport of particles along the longer time paths of the RTD (the right-hand log-normal distribution and the right-hand inset) begins to play a role. The effect is to broaden the PSD. The growth and mixing of particles travelling along the short and long-time paths represented by this two-mode RTD distribution produces a bimodal distribution of particles. Given enough time after the intermediate time range, most of the small grains in such a bimodal distribution will dissolve onto the larger ones. This changes the two-mode PSD into a single-mode PSD of larger mean size. For example, see Fig. 3, right-hand panel.

It is useful to compare the PSD for two different impeller arrangements of the 2000 l tank. In the first case the PSD results in a bottom-sweeping impeller tank are measured. Then the PSD resulting from a non-bottom sweeping arrangement. In Fig. 13 we present a typical electrolytical grain size analyzer (EGSA) derived PSD of a narrowly distributed set of microcrystals typically produced in the BDJ process with a bottom-sweeping impeller arrangement. The top graph displays the volume weighted distribution (third moment of the log-normal PSD) and the bottom graph gives the number-weighted distribution or simply PSD. The mean volume is 0.046 μm^3 and standard deviation of the log-normal distribution is 1.34 μm as estimated from more than 4000 electrolytic current pulses. As seen in the top panel of Fig. 13, the fine particles contribute little to the volume percentage of grains. However, as evident from the bottom panel of Fig. 13, their number percentage, of order 1–3%, in the range (0.001, 0.01) is significant.

We next investigate the effects of increasing the height of the impeller off the bottom of the tank. After seeding, the impeller is raised about 20 cm above the bottom, significantly less than half-way up the 2000 l tank as would be the case for the Rushton-type arrangement. The PSD result shown in Fig. 14 was obtained. The elevation of the impeller changes the large scale eddy flow structure resulting in two additional peaks at higher volume not present in the bottom sweeping impeller case (Fig. 13). Their presence was corroborated by electron microscopy. The difference in the two cases is due to the development of different secondary flows, i.e., due to the presence of a toroidal LSE below the raised
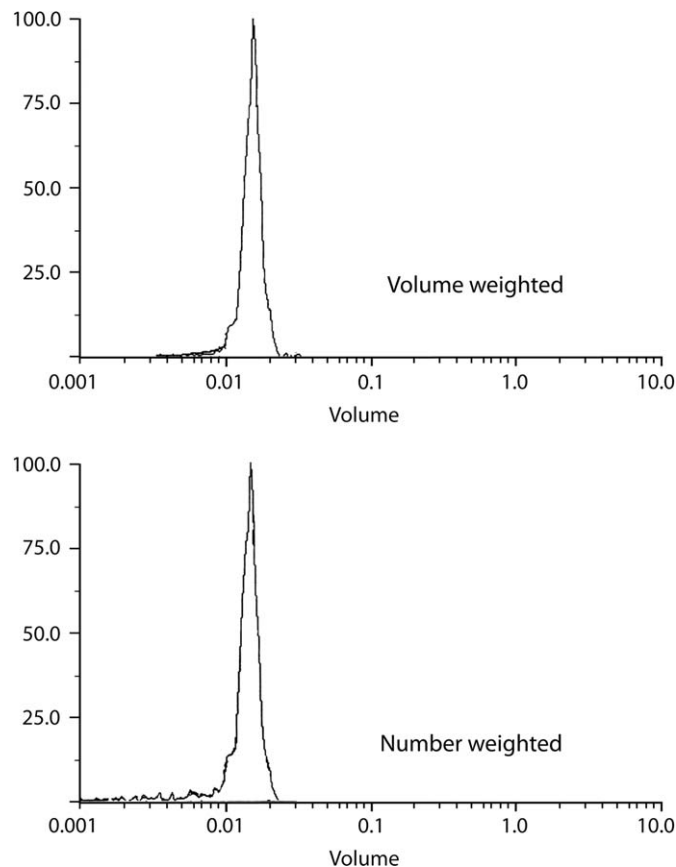

Fig. 13. Typical particle size distribution of crystallites produced in a bottom sweeping impeller crystallizer. Top panel is the volume weighted distribution, bottom panel is the number weighted PSD.

impeller. The PSD difference occurs even though the flow above the impeller in the two cases is similar.

Other effects corroborating the presence of secondary tori were also found in the 2000 l tank. An oscillatory variation in silver ion concentration (in terms of $pAg = -\log_{10}([Ag])$ was measured in the vertical direction approximately 15 cm away from the tank side walls. There was also a pAg variation in the horizontal direction as one moves from the tank walls to the center of the tank.

7. Summary and conclusions

This paper shows that regions of inhomogeneous flow and particle transport occur in a radial flow industrial bottom-sweeping batch crystallizer. These regions are toroidal large-scale eddies (LSEs). We show that flow in the LSEs and restrictions on particle transport through the stagnation surfaces bounding them is important to the particle size distribution produced in the crystallizer. The overall effect of the toroidal LSEs and their stagnation surfaces on the crystallization is to introduce an additional source of variability into the crystal growth. Experimental results for Lagrangian marker particle (LMP) trajectories are presented in terms of Poincaré sections, which reveal very clearly the structure of the flow. Further experiments using microconductivity probes show that the flow remains segregated long after the outer annulus is well-mixed.

Using a 280 l model mixing tank, it is demonstrated that stagnation surfaces can be identified using the Lagrangian marker particle (LMP) flow following technique. A cylindrical stagnation surface surrounding a central quiescent zone is found. The
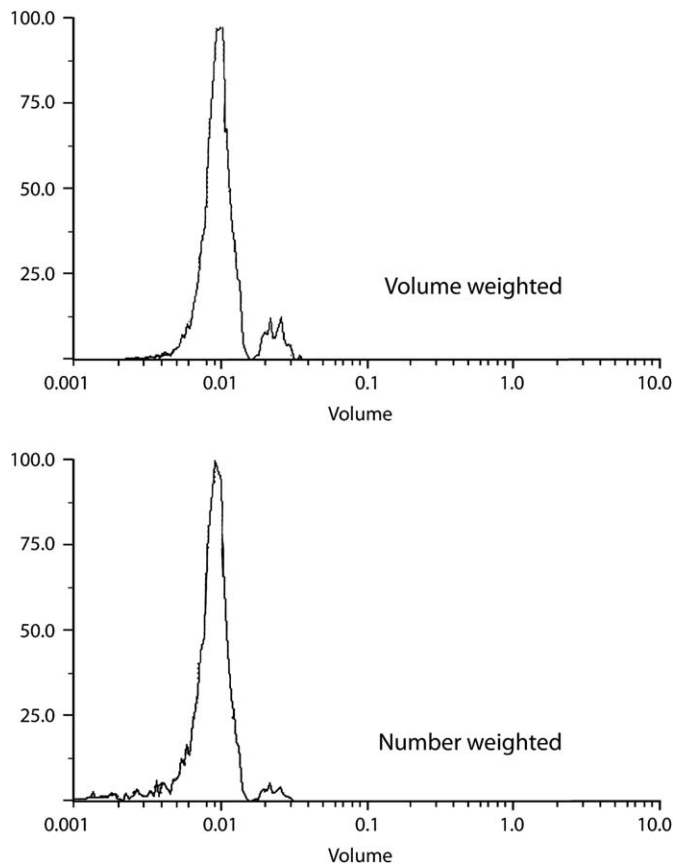
Fig. 14. Particle size distribution of crystallites produced with impeller elevated 20 cm from bottom. Top panel is the volume weighted distribution, bottom panel is the number weighted PSD.

inertially driven, upward perimeter swirl and central quiescent zone are easily identified in the Poincaré sections of the LMP trajectory. The upward perimeter swirl turns over at the top of the tank then develops into a down-welling flow that generates a stack of secondary toroidal LSEs concentric with the impeller shaft. These smaller tori build up as the tank is filled when operating in batch mode. The secondary toroidal structures can be identified by examining the detailed trajectories of the LMP.

The stagnation surface surrounding the central quiescent zone is found to be leaky at molecular scales as shown by micro-conductivity measurements. However, it is nearly impervious at the LMP scale (0.4 cm dia.). The size selectivity of the transport through the stagnation surfaces give rise to variable path histories and size-segregation of the growing crystallites. The resulting inhomogeneous particle transport can have a significant effect on the PSD, generally broadening it.

The combination of the Lagrangian marker particle (LMP) method, microconductivity, and the particle size measurement method (EGSA) applied to silver halide crystallization is useful for studying the effects of flow structure on the production silver halide microcrystals. It is clear that the present study can be extended to a parametric study including variation of impeller speed, LMP size, and diameter to height ratio. It would also be useful to perform the same measurements as a function of different static tank filling level and different rates of tank filling. Such a study would provide the data useful for future scale-up projects and for calibrating numerical simulations of crystal-lization. This would be especially useful when combined with a model of nucleation and growth of the microcrystals.

References

Allen, T., 1997. Particle Size Measurement, vols. 1 and 2. Chapman and Hall, Kluwer Academic, Norwell, MA.
Babiano, A., Cartwright, J.H.E., Piro, O., Provenzale, A., 2000. Dynamics of a small neutrally buoyant sphere in a fluid and targeting in hamiltonian systems. Phys. Rev. Lett. 84, 5764–5767.
Bai, G.E., Armenante, P.M., Plank, R.V., 2007. Experimental and computational determination of blend time in USP dissolution testing apparatus II. J. Pharm. Sci. 96, 3072–3086.
Brecevic, L., Skrtic, D., Garside, J., 1986. Transformation of calcium oxalate hydrates. J. Crystal Growth 74, 399–408.
Chow, L., 1996. Process for pulse flow double-jet precipitation. U.S. Patent 5,549,879.
Garside, J., Tavare, N.S., 1985. Mixing reaction and precipitation: limits of micromixing in an MSMPR crystallizer. Chem. Eng. Sci. 40, 1485–1493.
Gerber, A.M., 1982. Method for preparing photosensitive silver halide emulsions. U.S. Patent 4,332,887.
Haller, G., Sapsis, T., 2007. Where do inertial particles go in fluid flows. Physica D 237, 573–583.
Holland, A.B., Sawers, J.R., 1973. Grain size determination by electrolytic reduction. Photo. Sci. Eng. 17, 295.
Huq, P., Britter, R.E., 1995. Mixing of a two-layer scalar profile due to grid generated turbulence. J. Fluid Mech. 285, 17–40.
Kambe, T., 2004. Geometrical Theory of Dynamical Systems and Fluid Flows. World Scientific, Singapore.
Leubner, I.H., 2002. The balanced nucleation and growth model for controlled crystal size distribution. J. Dispersion Sci. Tech. 23, 577–590.
Maxey, M.R., Riley, J.J., 1983. Equation of motion for a small rigid sphere in a non-uniform flow. Phys. Fluids 26, 883–897.
Maxey, M.R., 1988. The gravitational settling of aerosol particles in homogeneous turbulence and random flow fields. J. Fluid Mech. 174, 441–465.
McLaughlin, J.B., 1988. Particle size effects on Lagrangian turbulence. Phys. Fluids 31, 2544–2553.
Moller, C., 1970. In: Proceedings of the International Congress on Photographic Science, Moscow, p. 125.
Mullin, J.W., 1997. Crystallization, third ed. Butterworth Heinemann, Oxford.
Mumaw, C.T., 1985. Process for pulsed flow, balanced double jet precipitation. U.S. Patent 4,539,290.
Nagata, S., 1975. Mixing: Principles and Applications. Hallstead Press.
Ottino, J.M., 1989. The kinematics of mixing: stretching, chaos and transport. Cambridge University Press, Cambridge.
Rielly, C.D., Marquis, A.J., 2001. A particle's eye view of crystallizer fluid mechanics. Chem. Eng. Sci. 56, 2475–2493.
Ruelle, D., Taken, F., 1971a. On the nature of turbulence. Commun. Math. Phys. 20, 167–192.
Ruelle, D., Takens, F., 1971b. Note concerning our paper: on the nature of turbulence. Commun. Math. Phys. 23, 343–344.
Scofield, D.F., Huq, P., 2009. Lagrangian marker particle trajectory and micro-conductivity measurements in a mixing tank. Chem. Eng. Sci. 64, 276–287.
Söhnel, O., Garside, J., 1992. Precipitation: Basic Principles and Industrial Applications. Butterworth-Heinemann, Oxford.
Tavare, N.S., 1989. Micromixing limits in an MSMPR crystallizer. Chem. Eng. Tech. 12, 1–11.
Tavare, N.S., 1995. Industrial Crystallization Process Simulation Analysis and Design. Plenum Press, New York.
Togatorop, A., Mann, R., Scofield, D.F., 1994. Application of CFD to inert and reactive tracer mixing in a batch stirred vessel. In: AIChE Symposium Series, vol. 299, pp. 19–32.
Wey, J.S., 1993. Batch crystallization. In: Myerson, A.S. (Ed.), Handbook of Industrial Crystallization. Butterworth-Heinemann, Boston, pp. 209–218.
Wittmer, S., 1996. Thèse, Charactérization du mélange dans une cuve agitée par trajectographie, L'Inst. Nat. Polytechnique de Lorraine, Nancy, France.
Wittmer, S., Vivier, H., Falk, H.L., Villermaux, J., 1995. Three-dimensional long-term particle tracking in a stirred tank. In: Seventh International Symposium on Flow Visualization, 11–14 September 1995, Seattle, Washington.